ARTICLE OPEN

Check for updates

Soil moisture-constrained East Asian Monsoon meridional patterns over China from observations

Waheed Ullah [1], Chenxia Zhu[1], Guojie Wang [1 ✉], Daniel Fiifi Tawia Hagan[1], Dan Lou[1], Jiangfeng Wei[2], Aisha Karim[1], Shijie Li[1], Buda Su[1] and Tong Jiang[1]

As an internal forcing of the earth climate system, soil moisture (SM) significantly influences the water and energy cycle by controlling evapotranspiration and terrestrial solar energy. The current study used observed precipitation, remotely sensed SM, and reanalysis of atmosphere and land parameters to assess the East Asian Monsoon (EAM) precipitation variability due to meridional SM oscillations across China. A generalized linear method, namely coupled manifold technique (CMT) for assessing the reciprocal forcing between two climate fields and numerical simulations are applied to SM and EAM precipitation. We find that the EAM precipitation interannual variability between north and south China significantly correlates with SM meridional oscillation. The CMT results further showed that SM forcing has a significant (99% confidence) influence on the EAM precipitation explaining about 0.40 of the variance ratio in north and south China. The EAM and SM composite analysis show that the wetter (drier) north (south) oscillates the EAM precipitation over the north (south) of China and vice versa due to SM thermal controls. We then used control and sensitivity simulations with SM observations to further validate the findings implying that SM can potentially improve the interannual EAM forecast skills. The model results show that a wetter (drier) north (south) results in negative (positive) sensible heat (latent heat) anomalies that impact the boundary layer and propagate to change the meridional atmospheric heating profile. When positive (negative) SM anomalies exist over northern (southern) China, the zonal easterlies and extratropical westerlies move to north China causing above-normal precipitation that descends into southern China, suppressing subtropical westerlies and precipitation in southern China. On the contrary, a dry (wet) north (south) favors intensified subtropical westerlies and precipitation in southern China. The findings have dire implications for the water and energy cycle of the region in the projected wetting and drying patterns of the north (south).

INTRODUCTION

The complex structure of the East Asian Monsoon (EAM) precipitation extremes poses direct threats to China's regional economy and Gross Domestic Product (GDP). The EAM complexity lies within its drivers, which consist of internal feedback between different components of the earth's climate system, including land[1–3], atmosphere[4,5], Ocean[6], and cryosphere[7,8]. The interannual variability of the EAM could be understood as a direct space-time precipitation variation between (within) the northern and southern major river basins of China forced by these factors. The anomalous modes of these driving factors influence the precipitation extremes that produce floods, droughts, and heatwaves with profound socioeconomic impacts[9]. The severity, frequency, and intensity of floods and droughts may amplify the regional losses to $60 billion in capital and many folds attributed to drought under 1.5 and 2 °C warmings[6,10,11]. The historical EAM precipitation-induced flooding during 1984–2018 cost $19.2 billion, accounting for 0.5% of the national GDP and 54% of total weather-related losses, with an exponential increase from 2006-onward, accounting for $25.3 billion[10]. In >1.5 °C warming of the climate, the EAM may intensify primarily due to enhanced land-sea thermal contrast favoring increased continental precipitation[12,13]. The projected increase in the mean and frequency of the precipitation extremes makes the EAM domain one of the extreme flood-prone regions later in the twenty-first century[10,14].

The coherent monsoon variability and its quantitative response to the earth system's internal and external feedback have been an ongoing research topic in recent decades[15,16]. The global monsoon system functions as a three-dimensional planetary-scale circulation primarily driven by solar insolation as an external forcing oscillating precipitation band across hemispheres[17]. The internal forcing and feedback within the earth spheres further drive the monsoon's spatial distribution and shape, including the ocean's coupled processes, overlying atmosphere, and land-sea distribution[18,19]. These forcing alto-gether result in coupled processes and modes influencing monsoon characteristics from synoptic to mesoscale, including the onset, advance, and retreat[20,21]. Past efforts have highlighted multiple dimensions of EAM, including its onset[22], meridional oscillations[23,24], and regional flooding/droughts[6] due to interactions (modes) of the land-atmosphere and ocean nexus (processes). The EAM characteristics described above are shaped by these coupled modes within the earth system, benefiting the forecast and prediction skills. Zhou et al. (2021) reported the mediating role of SST in offsetting the spring SM influence of summer EAM precipitation with decreased precipitation under positive SST background and vice versa for negative SST, further reducing the spatial spread of precipitation anomalies[1]. Lv et al. (2019) reported an increase in the maximum daily precipitation during the Eastern Pacific *El Niño* and Central Pacific *El Niño*

[1]Collaborative Innovation Center on Forecast and Evaluation of Meteorological Disasters (CIC–FEMD), Nanjing University of Information Science and Technology (NUIST), Nanjing 210044, China. [2]Collaborative Innovation Center on Forecast and Evaluation of Meteorological Disasters/Key Laboratory of Meteorological Disaster, Ministry of Education/International Joint Research Laboratory on Climate and Environment Change, Nanjing University of Information Science and Technology, Nanjing 210044, China. ✉email: gwang@nuist.edu.cn

decaying years and *La Niña* developing years[25]. The understanding of the oceanic forcing mechanism impact on the EAM for flood hazard assessment is still limited and subject to uncertainties[6,9]. These skills could be further improved considering the impacts of SM space-time variability as an additional slowly evolving/decaying mode of earth's climate system affecting the water and energy cycle even in the absence of the oceanic forcing[2,26].

The intrinsic memory of SM over days to weeks and months[27] can be an added skill if considered in the forecast and predictability with probabilistic outcomes of its relationship with the climate field[2,28–30]. In regions where oceanic modes are the precursors of climate variability, SM variability exhibits positive feedback loops influencing energy and water cycle. In the absence of such oceanic modes;[31,32] SM becomes the second essential climate variable after SST[30,33,34]. Through physical processes, a dry(wet) SM impacts the immediate surface warming(cooling) through sensible (latent) heat fluxes[27,29,30], impacting the diabatic heating and divergent circulations[28,29]. Studies have further suggested that SM anomalies may trigger certain circulation patterns (stationary and quasi-resonant waves) with geographically varied impacts, including heatwaves[35,36] due to SM-temperature coupling adding more SH to the boundary layer amplifying the heatwave intensity and duration. Through interaction with the overlying atmospheric circulation, SM anomalies can drive the Rossby wave train influencing the remote climate field and inducing floods[37–39].

Over the EAM domain, Shi et al. (2021) reported significant sensitivity of the atmospheric circulations and precipitation to SM in a weakly coupled model posing a dipole with wetter north and drier south[2]. Gao et al. (2019), from a suite of model simulations and observations, showed that the spring SM interacts with EAM precipitation involving SM coupling with atmospheric circulations[23]. Dong et al. (2022) found a negative relationship between July SM and August precipitation over EAM, highlighting SM controls over atmospheric condensation and heating[40]. Bao et al. (2010) showed that the inclusion of remotely sensed SM in an atmospheric model could improve the monsoon onset mainly due to its ability of a realistic representation of land-ocean thermal contrast[41]. Meng et al. (2018) showed significant control of SM over precipitation over the Tibetan Plateau and concluded that a wetting trend of the plateau would increase precipitation[42]. Wei et al. (2019; 2012) showed that the northern EAM precipitation is sensitive to local ET due to strong land-atmosphere interactions[43,44]. These studies show that SM, after SST, is a key component in the EAM precipitation variability due to its constraints on evapotranspiration, surface energy fluxes, and diabatic heating maintains a land-ocean thermal gradient that affects the EAM precipitation. However, the role of SM is generally described as a probabilistic, process-oriented indicator lacking quantification and the physical mechanism of its regional space-time variability and its control over the local and remote climate. The availability and application of observations are rather limited and commonly replaced by reanalysis data[34,45]. The quality and inconsistent model structure are other constraints that often undermine the land surface and energy balance approximation when coupled with the atmosphere[7,34,46,47]. The key question for further understanding thus is: how can SM meridional oscillation between the north and south China key climate regions[40,48] be used to predict the interannual EAM precipitation variability. Conversely, what is the variance ratio of the EAM precipitation sensitive to the meridional SM oscillation, and what are the underlying mechanisms connecting SM anomalies with large-scale circulation and moisture flux source changes? To answer these questions, in this study, we first derived the relationship between SM meridional variability and its effect on the EAM precipitation oscillation between the north and south China river basins. Then a potential mechanism from the effect of SM anomalies on the surface energy fluxes, diabatic heating, and circulations is investigated as a consequence of SM meridional oscillation affecting the EAM precipitation. Our approach is based on a robust generalized linear statistical tool[32,49] that quantifies the JJA precipitation spatiotemporal variability due to SM. We then used a coupled regional climate model with a physically based configuration constrained with the same observed SM to preserve and replicate its effect on the water and energy cycle. Such an approach identifies the possible mechanisms that drive the EAM precipitation sensitivity to JJA SM meridional oscillation.

Study area description

The geographical distribution of the Asian monsoon domain over East Asia (China) can be classified into three sub-systems: the WNP-monsoon in southeast China, EAM in north China, and the South Asian monsoon in southwest China. The EAM domain (Supplementary Fig. 2a, b) hydrometeorological cycle is primarily due to maximum precipitation from June to August, termed the monsoon season (Supplementary Fig. 1c). The EAM precipitation band oscillations across China indicate a wet north and south dry and vice versa reflected in the diverse climate classes (Supplementary Fig. 1)[50]. The interannual variability of the EAM onset and precipitation variability is subjected to changes in multiple atmospheric, oceanic, and land surface processes extensively studied in previous studies[3,17,51–53]. The broad-scale EAM onset includes a regional connection of the tropical and subtropical westerlies into the South China Sea (SCS) to the north of the subtropical high, replacing the Western pacific subtropical ridge[54]. During this process, the westerlies establishment over SCS initiates monsoon onset followed by the Mei-Yu/Baiu rainband initiation results in EAM regional monsoon onset from late April to early May[21,54]. Global warming is expected to enhance the land-ocean thermal contrast intensifying the earlier Asian monsoon onset and changes in the sub-seasonal and spatial precipitation pattern that need in-depth exploration[10,11,55,56].

RESULTS

Soil moisture relationship with precipitation from observations

The empirical orthogonal function (EOF) analysis of EAM precipitation shows a meridional oscillation of precipitation, characterizing 48% of the total variance (Fig. 1a, b). The meridional precipitation band oscillation results from the complex interplay of oceanic and land surface processes[6,17,57] developed from their modes of behaviors resulting from their memory shaped by anomalous energy fluxes. The leading EOF mode eigenvectors and principal component (PC1) show spatiotemporal precipitation variability across East China's south and northern river basins (Supplementary Fig. 1).

There is a lack of consensus on the definitive physical process's relative role in shaping and maintaining the precipitation meridional dipole pattern concerning the ocean and SM as mediators of land surface processes. Here we attempted to use SM as an additional factor for assessing the meridional EAM precipitation variability changes. We used the Pearson correlation technique to correlate the PC1 (Fig. 1b) with the SM interannual variability during the monsoon season. The results (Fig. 1c) show a significant (95% confidence) correlation between the PC1 and SM over the EAM domain. The correlation strength exhibited a similar meridional dipole with precipitation EOF showing negative coefficients (<-0.60) in the north, including the northern Yangtze River basin, the Yellow River basin, the Haihe River, and northeast China. The regions in south China, including the southern Yangtze River basin, Pearl River basin, and adjacent southern regions, show positive correlation coefficients between the PC1 and SM (>0.65). The space and time variability of EOF and correlation coefficients
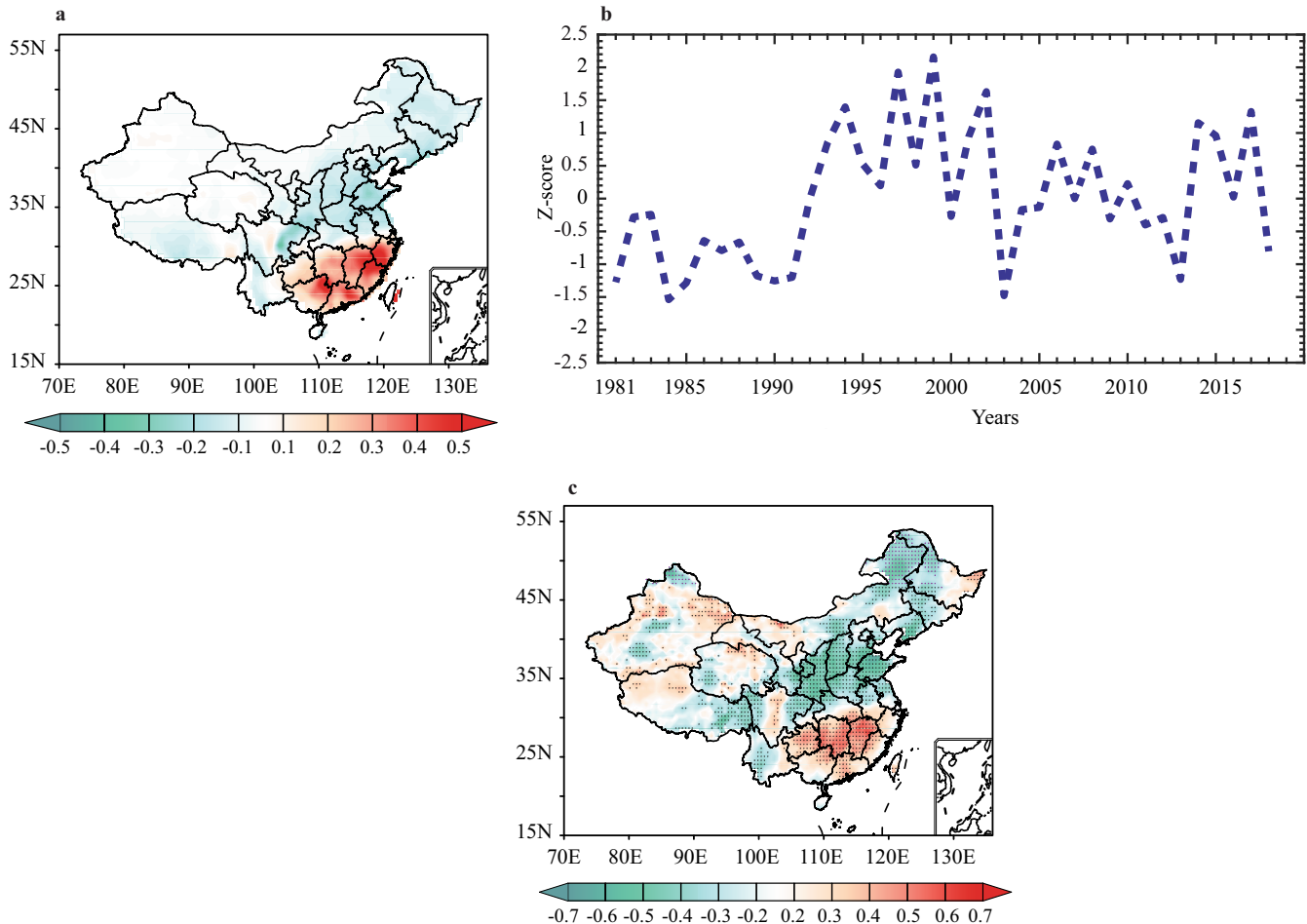
Fig. 1 **Spatiotemporal JJA precipitation variability and its relationship with soil moisture.** The **a** EOF eigenvectors and the **b** leading principal component (PC1) of the JJA precipitation from 1981 to 2018. The **c** pixel-wise correlation of the PC1 and JJA SM during 1981-2018. The dotted regions have passed the significance test with a 95% confidence bound.

infer that the EAM precipitation meridional oscillation is strongly linked to SM anomalies. The results imply that relatively higher SM in the northern transitional parts of China will result in relatively higher precipitation in the northern Yangtze River basin, Haihe and Huaihe River basins, and vice versa in southern China. The influence of SM on the EAM meridional precipitation oscillation is further quantified using a robust Coupled Manifold Technique (CMT) that separates the variance ratio of precipitation connected to SM[32,49]. Figure 2 shows the fraction of EAM JJA precipitation (Fig. 2a) that is forced by JJA SM interannual variability, leading mode of the forced precipitation (Fig. 2b), and standardized PC1 of the forced precipitation leading mode and SMI (Fig. 2c). To ensure that the SM forced precipitation is not by chance, we performed an additional significance test using Monter Carlo simulations of 1000 repetitions with a significance of 1% for the shaded regions.

The results (Fig. 2a) show that SM interannual variability forces a significant (99% confidence bound) fraction of EAM JJA precipitation. The variance ratio is relatively higher in northern China, including the Huaihe, Haihe River basin (0.38), southern Yangtze River basin (0.37), and Tibetan plateau (0.32). The EOF (Fig. 2b) of the forced precipitation leading mode shows 63% of the total variance attributed to SM variability with an obvious dipole pattern. The SM forcing is relatively higher in those EAM regions where the EOF inferred a strong spatiotemporal variability (Fig. 1), implying that SM is an evident component forcing the EAM precipitation interannual variability between the north and

southern China river basin[2]. To isolate the SM control, we calculated a soil moisture index (SMI) using the northern regional area-averaged (35°−44°N, 99°−120°E) SM and subtracted the southern region (22°−31°N, 99°−120°E) area-averaged SM from it. Positive (negative) SMI implies wetter (drier) conditions over the north and vice versa for the south. The PC1 and SMI (Fig. 2c) show phase-opposite dynamics with a significant negative correlation (−0.62) inferred from interannual variability. This implies that a positive SMI would drive the EAM precipitation band to the northern river basins and vice versa for the negative SMI evident from the PC1 and eigenvectors of the forced precipitation. An evident anomalous PC1 and SMI interannual variability further support that the strength of the SMI directly correlates with the EAM meridional intensity during the study period, which agrees with (Liu et al. 2017)[58] stating that spring precipitation-induced summer SM memory can affect the strength of EAM.

Altogether, the eigenvectors spatial pattern, PC1, and SMI suggest an intrinsic relationship between SM and precipitation during the study period. Spatially, the SM magnitude in time has shown changes followed by precipitation band oscillations and variability between north and south China. We based the SM coupling with EAM precipitation on a composite analysis to link SM variability and its impact on the boundary layer processes and atmospheric circulations. For this purpose, six years with positive standard deviations (1988, 1990, 1996, 2003, 2004, and 2011) and seven years with negative standard deviations (1982, 1997, 1999, 2001, 2002, 2015, and 2017) of the SM forced
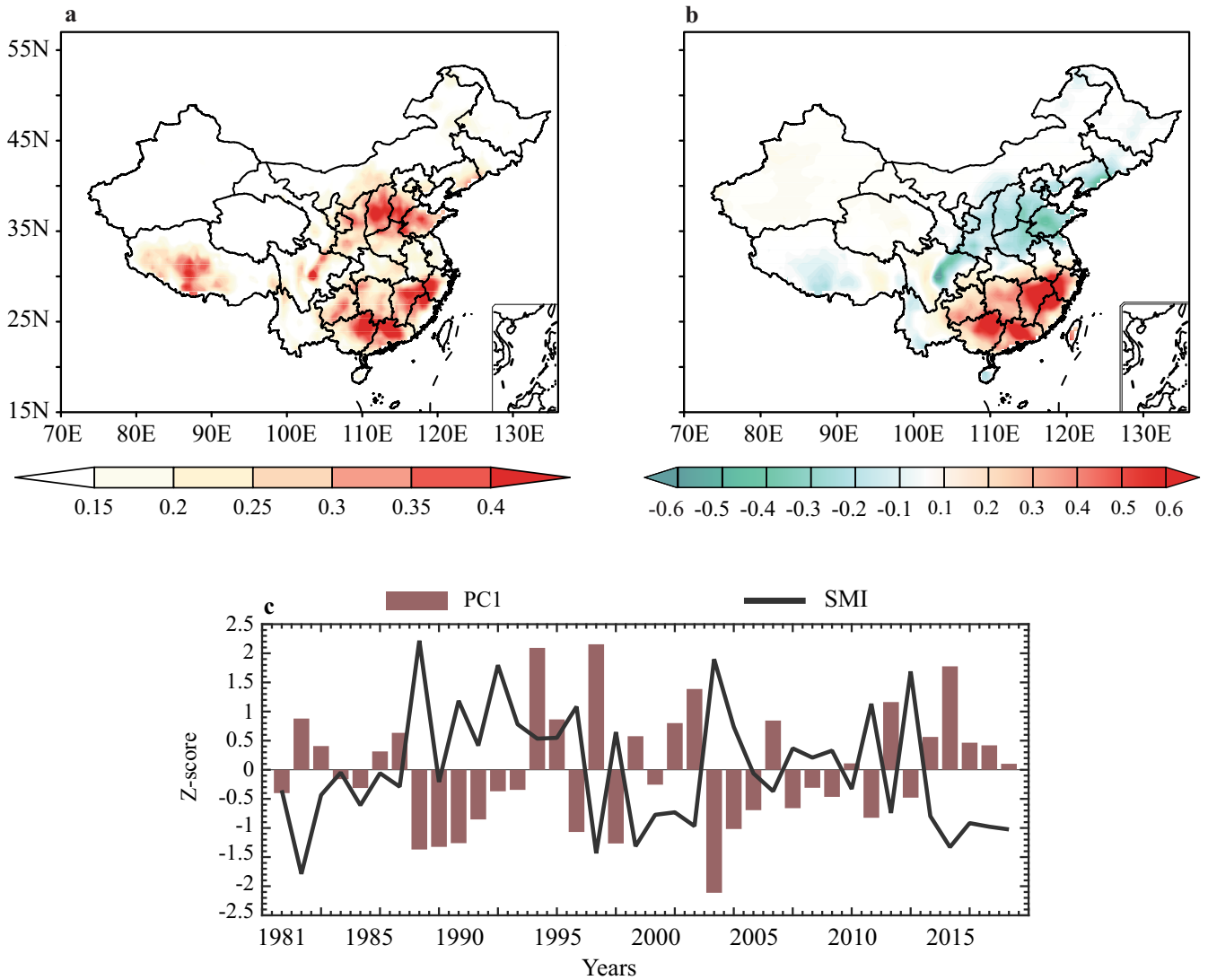
Fig. 2 The SM forced precipitation variance ratio meridional variability. The **a** fraction of EAM (JJA) precipitation (unit: mm) forced by JJA SM (unit: $m^3 \, m^{-3}$), the **b** eigenvectors of the forced precipitation leading mode, and the **c** PC1 and SMI during 1981–2018. The forced precipitation leading mode variance is 63%, whereas the PC1 and SMI are negatively correlated (−0.62) with a significance bound of 95%.

precipitation PC1, and SMI (Fig. 2c) is selected. These composites are selected where their standardized values exceed ±1, providing the confidence to explain the associated surface and atmospheric circulation anomalies.

Figure 3 shows the composite anomalies of the SM and precipitation during the positive (SMI$_{wet}$ hereon) and negative (SMI$_{dry}$ hereon) composite years. During the SMI$_{wet}$ composite (Fig. 3a), significant positive SM anomalies ($0.02 \, m^3 \, m^{-3}$) are evident north of the Yangtze River basin, stretching to the Yellow and Huaihe River basins. At the same time, the southern Yangtze River basin to the Pearl River basin show negative SM anomalies ($-0.03 \, m^3 \, m^{-3}$). During the SMI$_{dry}$ composite (Fig. 3b), the SM dipole has spatially reversed with negative anomalies ($-0.02 \, m^3 \, m^{-3}$) in the northern River basins and Yangtze River basin. The southern Yangtze River and Pearl River basins have also exhibited positive SM anomalies ($0.03 \, m^3 \, m^{-3}$). The precipitation anomalies during the SMI$_{wet}$ composite (Fig. 3c) have exhibited positive anomalies (40 mm) in the northern Yangtze River basin, Yellow River basin, and Huaihe River basin. The southern Yangtze River basin and the rest of southern China show negative precipitation anomalies (−40 mm). During the SMI$_{dry}$ composite (Fig. 3d), significant precipitation anomalies are evident in a

relatively larger spatial domain with negative anomalies (−45 mm) in the north and positive anomalies in the south (50 mm).

Positive(negative) SM anomalies in the north(south) result in more(less) precipitation in the northern(southern) River basins of China and vice versa. The spatial patterns of the SM and precipitation anomalies geographically have significant differences where SM anomalies are located farther north than corresponding precipitation anomalies. The strength of the SM anomalies is rather stronger in the dry-arid northern regions and wet-to-humid southern regions; the precipitation anomalies in response oscillate between the northern transitional and southern humid zone. The SM meridional anomalous pattern impacts the surface energy fluxes with SH(LH) negative(positive) anomalies (Supplementary Fig. 4), impacting the boundary layer thickness (Supplementary Fig. 5a) and vertical diabatic heating through condensation from the latent heating (Supplementary Fig. 5b). Such SM-thermal controls intensify the nature of the land-atmosphere interactions more vigorously in the monsoon regions[2], substantially controlling the tropical to extratropical Pacific zonal easterlies and midlatitude westerlies circulations anomalies, modifying the moisture transport that can meridionally oscillate the precipitation (Supplementary Fig. 5c, d). SM mediation in land-atmosphere coupling is
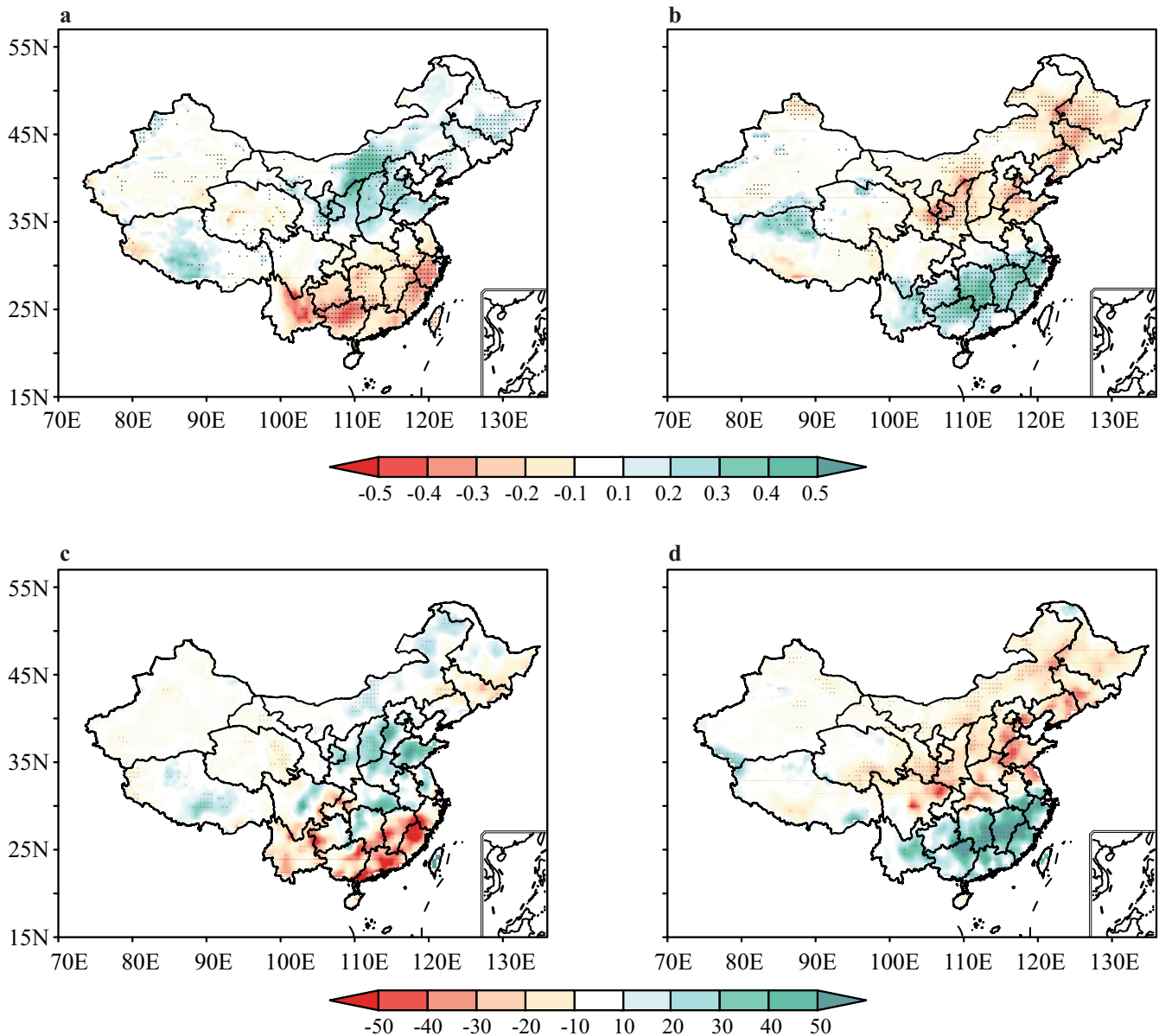
Fig. 3 The SM and precipitation composite anomalies. The **a, b** SM (unit: (m^3 m^{-3})*10^2) and **c, d** precipitation (unit: mm) anomalies for the **a, c** SMI$_{wet}$ and **b, d** SMI$_{dry}$ composite. The stippling indicates significant (95% confidence) composite differences from the mean interannual field during 1981–2018.

portrayed to perturb the atmospheric circulations through its thermodynamic propagation of surface energy fluxes that partly contribute to 65% of the global continental precipitation recycling[2,59]. Over the EAM domain, efforts have been made to assess the land-atmosphere coupling as a function of SM sensitivity using observations and regional climate and forecast model experiments[2,40,60]. Here we conducted a control and sensitivity experiment with observed soil moisture from remotely sensed sources to identify the potential mechanisms leading to the relationship between SM and EAM precipitation meridional oscillations above.

Observations constrained model simulations

Figure 4 shows the daily SM standard deviation differences between (Fig. 4a) SM$_{ECV}$ and SM$_{CLIM}$ for 2000–2018. Geographically, the standard deviation between the two simulations is larger (>75 kg m^{-2}) in northern and southern China. Higher standard

deviations in the SM$_{ECV}$ run indicate regions where we expect stronger SM sensitivity and control over the coupled land-atmosphere processes. Figure 4a shows that the impact of SM over EAM is dominant over East China, where the observations also show significant dry and wet precipitation meridional patterns. From a climate perspective, the dry, arid, and transitional regions in the north and northern Yangtze River basin and southern China (Supplementary Fig. 1) differ in daily soil moisture variation. The results indicate that the SM initializations scheme used here can characterize both the model seasonal and interannual variations with distinctly larger variability (sensitivity) in SM$_{ECV}$. The SM (both SM$_{ECV}$ and SM$_{CLIM}$) simulations over a small region from the Yangtze River basin show an obvious difference at seasonal and interannual scale for total (Fig. 4b, d) and surface (Fig. 4c) SM. The SM climatologies (Fig. 4c, d) are consistent, but the strength of variability between SM$_{ECV}$ and SM$_{CLIM}$ is used to assess their difference in interacting with the atmosphere[61]. The model surface and atmospheric variables (Supplementary Fig. 5)
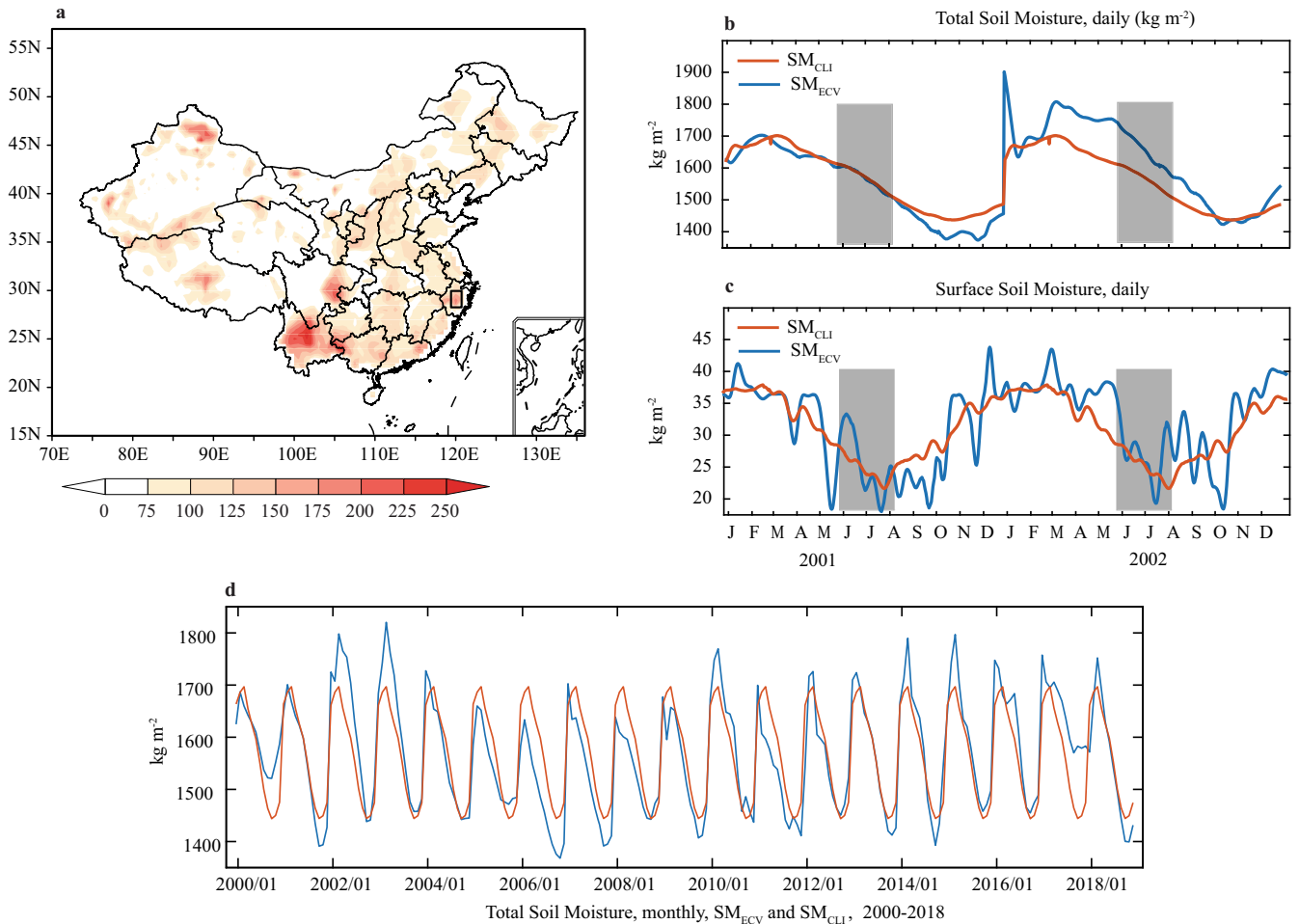
Fig. 4 The spatiotemporal variability and deviation of SM between the SM$_{ECV}$ and SM$_{CLIM}$ simulations. The difference in the **a** Standard deviation of daily total-column SM between SM$_{ECV}$ and SM$_{CLIM}$ (unit: kg m^{-2}) over 2000–2018. **b** Monthly evolution of the area average [118°–121°E: 28°–30°N] SM from 2001 to 2002. **c** Daily total surface SM values over two seasonal cycles (2001–2002) and **d** monthly total SM.

difference between the SM$_{ECV}$ and SM$_{CLM}$ results in drier conditions over Northeast China and wetter conditions over South-east China, implying underestimations over the Northeast China and overestimations over the Yangtze River basin and southeastern China. Such biases are previously reported over the study region due to the model and boundary layer uncertainties, including the topographic effects[7,40].

Figure 5 shows SMI$_{wet}$ (2003, 2004, 2011) and SMI$_{dry}$ (2001, 2002, 2015, 2017) composite difference of SM$_{ECV}$ and SM$_{CLIM}$ based on model simulation during 2000 to 2018. The difference between the two simulations is calculated by subtracting the mean precipitation of SM$_{CLIM}$ from SM$_{ECV}$. The SH differences for SMI$_{wet}$ (Fig. 5a) show a decreased sensible heat (SH) (-10 W m^{-2}) in the northern parts of China, followed by an increase (12 W m^{-2}) in the south. The latent heat (LH) (Fig. 5c) magnitude during SMI$_{wet}$ is higher (12 W m^{-2}) in the north and vice versa in the south. The SH is weaker in northern China during the SMI$_{dry}$ composite (Fig. 5b), and moderate negative values (-6 W m^{-2}) are obvious in southern China. The LH (Fig. 5d) during SMI$_{dry}$ shows a moderate increase in the north, and its mean magnitude in the south has shown an obvious increase. The SMI composite difference of the north and south fluctuated the near-surface energy balance, with an above-normal SM profile and positive LH due to changes in SM. From the meridional oscillation of the SMI between the north and southern parts of China, the typical land-atmosphere hot-spots regions may also shift towards the north, driven by SM in the transition and arid dry north.

During the SMI$_{wet}$ composite (Fig. 5e), relatively higher precipitation in northern China (110 mm) and decreased precipitation in southern China (-80 mm) is evident. During the SMI$_{dry}$ composite (Fig. 5f), the precipitation differences between north and southern China have shown a shift contrary to the SMI$_{wet}$ composite. Regional biases in the spatial pattern are evident due to the model uncertainties, topography, and regional sensitivity to oceanic forcing in the south[1,7]. The precipitation difference between SM$_{ECV}$ and SM$_{CLIM}$ validates the diagnostic results in Fig. 3, inferring that the SM meridional dipole impacts the precipitation oscillation between north and south China. The associated mechanism from the large-scale circulations is further shown to imply the role of SM in modifying the atmospheric circulation pattern and precipitation magnitude. During the SMI$_{wet}$ composite (Fig. 5g), the difference between wind components (vectors) and vertical velocity (shaded) shows intensified wester-lies merging into the cyclonic pattern over the east coast of China. The moderate extra tropical westerlies and midlatitudes north westerlies are ascending towards northern China, resulting in above-normal precipitation as shown in the diagnostics. The Pacific zonal easterlies from the subtropical region descend into southern China with a stratified atmosphere suppressing the precipitation. During the SMI$_{dry}$ composite (Fig. 5h), the cyclone pattern during SMI$_{wet}$ has moved towards the southeast, with its leading ridge descending into northern China, suppressing the precipitation. The moderate subtropical westerlies are now evident in the Bay of Bengal, moving towards the Yangtze River
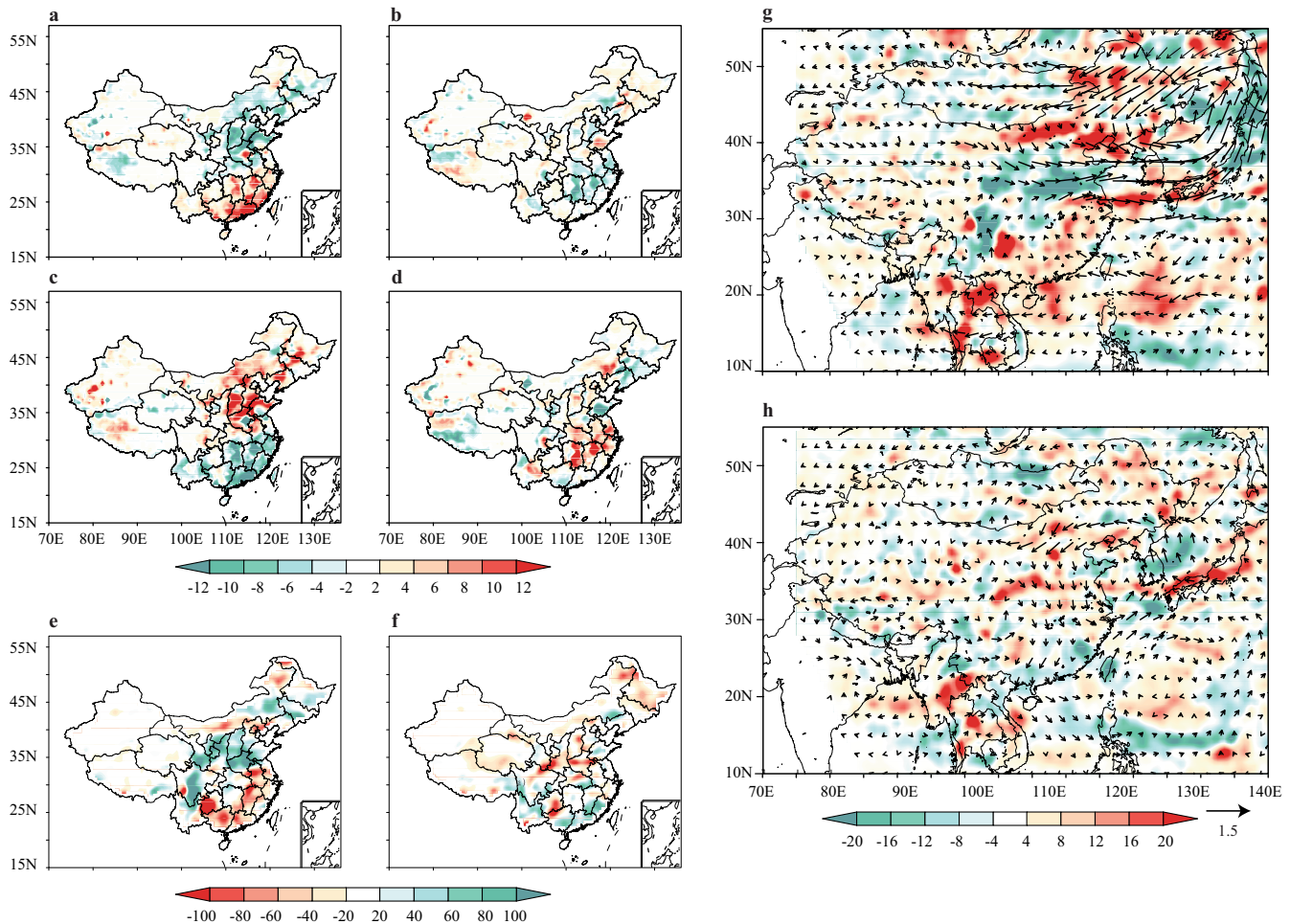
Fig. 5 The composite difference of surface energy fluxes, precipitation, and atmospheric variables for SM$_{ECV}$ and SM$_{CLIM}$ simulations. The composite difference of **a**, **b** SH, **c**, **d** LH fluxes (unit: W m^{-2}), **e**, **f** precipitation, and **g**, **h** 500 hPa wind (vectors) and vertical velocity (shaded) (unit: ω*10^{-2} Pa s^{-1}) for (**a**, **c**, **e**, **g**) SMI$_{wet}$ and (**b**, **d**, **f**, **h**) SMI$_{dry}$. The composite differences are calculated by subtracting the SM$_{CLIM}$ composites from SM$_{ECV}$ composites.

basin and south China. The descending ridge of the cyclone from the north and the subtropical westerlies resulted in enhanced precipitation over southern China and suppressed precipitation in northern China.

DISCUSSION

The East Asian monsoon (EAM) precipitation space-time changes are partly driven by the feedback and teleconnections of the atmosphere with the ocean and land. Studies have investigated that the SM local and remote control[23,40], and the ocean-induced tropospheric circulations, synoptic evolution, and teleconnection[6,17,24] are the major drivers of the EAM precipitation space-time variability. Our statistical assessment and model simulations show that SM meridional oscillations affect the EAM precipitation band oscillation over China. Conversely, positive (negative) SM anomalies over northern (southern) China river basins (Supplementary Fig. 1) are related to more (less) precipitation in the north(south) of China. The composite analysis shows that SM meridional variability impacts the near-surface energy fluxes and PBL dynamics (Supplementary Figs. 4, 5), intensifying the nature of the land-atmosphere interactions more vigorously in the monsoon regions[2] and affecting the vertical thermal column of the atmosphere[28,29]. The results imply that positive SM anomalies in northern river basins would impact atmospheric diabatic heating through the latent heating of condensation. Due to the

energy-limited regime of the southern river basins, atmospheric diabatic heating may have less sensitivity to the SM anomalies, as explored globally[28,29,62]. The SM-thermal controls during SMI$_{wet}$ intensify the extratropical Pacific easterlies and midlatitude westerlies over northern river basins as the primary moisture flux source (Supplementary Fig. 5); BOB is the primary moisture source of precipitation over southern China during the SMI$_{dry}$ composite. The numerical simulation further validated the proposed mechanism implying that the meridional SM pattern impacts the precipitation band accordingly, with a wetter north resulting in more EAM precipitation than the south and vice versa. When SM anomalies are stronger in the dry northern and wet to humid southern parts, the precipitation anomalies have shown widespread meridional oscillation between the northern transitional and southern humid zones[2,63–65]. Our findings are consistent with Shi et al. (2021), that SM potentially influences the EAM precipitation[2], and Dong et al. (2022), who further reported that a negative SM anomaly in southern China results in positive precipitation anomalies in Huang–Huai–River basin involving the remote SM effect[40]. Another study by Liu et al. (2017) proposed that more (less) spring precipitation over eastern (southern) China results in more(less) summer precipitation over north(south) China due to SM memory that can affect the strength of the EAM[58]. Similar attempts have further shown that EAM precipitation is dominantly controlled by SM at multiple timescales, surpassing the strength of oceanic forcing[1] and that the SM variability

influences the EAM strength[63]. Our study further concludes that the SM meridional oscillation can drive the EAM precipitation band across the major river basins of eastern China due to changes in circulation patterns and associated moisture flux sources affecting the strength of EAM. The SM thermal controls modulate the boundary layer processes affecting the circulation patterns in the tropical Pacific, BOB, and mid-latitudes. The findings have practical implications for skillful interannual predictions of EAM precipitation for drought and floodings in the northern and southern major river basins under climate change. Similarly, north and southern China's historical drying and projected wetting would have contrasting consequences for the regional-scale hydrological cycle, cropping pattern, land use, flood, and drought[11,66–68]. The drying of the northern river basins[69] would suffer from drought and temperature extremes due to SM-Temperature coupling;[70,71] the SM meridional oscillation-induced flood risk could increase in the wetter south due to enhanced moisture flux transport as identified by Xia et al. (2022)[72]. The limiting factors of the current study could range from boundary layer and topography-induced biases, and numerical model-induced uncertainties. The complex relationship between the SM meridional oscillation and its effect on EAM needs to be studied jointly with the oceanic forcing to counter floods, droughts, and extreme climate hazards[6,73].

METHODS

Datasets

The datasets used in this study include soil moisture from the European Space Agency-Essential Climate Variable (ESA-ECV SM), precipitation data from the China Meteorological Administration (CMA), and European Medium-Range Weather Forecasts (ECMWF) ReAnalysis 5th generation ERA5 reanalysis. The study's time scale is from 1981 to 2018 based on precipitation and SM data availability, whereas the numerical simulation is from 2000 to 2018 when ESA-ECV SM benefits from maximum satellite retrieval inputs[74]. The CMA precipitation is produced from 2474 meteorological stations across China, with maximum station density in eastern China[75,76]. The data is produced using a thin-plate spline technique involving the elevation-based uncertainty adjustment using the Global 30-Arc Second Digital Elevation Model (GTOPO30 DEM). The dataset is gridded at $0.5° \times 0.5°$ resolution and has been widely used in multiple studies to assess changes and variability in water cycles and other meteorological fields[75]. The ESA-ECV SM data developed under their Climate Change Initiative is developed using the dual-channel VU University Amsterdam-National Aeronautics and Space Administration (VU-NASA) Land Parameter Retrieval Model (LPRM) that converts the brightness temperature of multiple sensors into surface SM[77]. The current study used volumetric soil moisture contents ($m^3 m^{-3}$) at a resampled spatial resolution of 50 km for June, July, and August during 1981–2018, which was interpolated using a three-dimensional gap-filling approach[78]. The ERA5 from ECMWF is used for the surface and atmospheric variables[79]. ERA5 provides hourly estimates of the land surface and atmospheric variables at a relatively higher horizontal resolution of 31 km and 137 vertical levels. The improvements and advances in ERA5 include improved tropospheric circulations, observations from newer satellites, and more[80]. The ERA5 SM was used as a reference to rescale the ECV SM based on CDF matching because of the reported good skill of ERA5 in capturing SM dynamics[81] and confining it within the water and energy balances of the later model simulation.

Coupled Manifold Technique

The Couple Manifold Technique (CMT)[49] explains the connected variability between two climatic fields, considering their spatial and temporal variability. It decomposes a climate field into two

portions of variability; the first portion denotes the variability forced in a statistical sense by the other field, and the second is free from the other field. Assuming two climate fields, **Z** and **S**, each field can be decomposed into two separate sub-fields (Eqs. 1, 2) called free and forced manifolds, respectively. In Eqs. 3 and 4, A and B express the linear relationship between the **Z** and **S** fields. **A** expresses the effect of **S** on **Z**, and **B** expresses the effect of **Z** on **S**. The subscripts 'free' and 'for' denote the components of **Z** and **S** fields free from or forced by the other field, which is derived using Procrustes minimization problem[82] respectively.

$$\mathbf{Z} = \mathbf{Z}_{for} + \mathbf{Z}_{free} = \mathbf{AS} + \mathbf{Z}_{free} \tag{1}$$

$$\mathbf{S} = \mathbf{S}_{for} + \mathbf{S}_{free} = \mathbf{BZ} + \mathbf{S}_{free} \tag{2}$$

The fraction of the **Z** field's variance forced by the **S** field is then derived using Eq. 3, whereas, for the **S** field, the variance forced by the **Z** field is derived from Eq. 5, respectively[83].

$$\mathbf{Z}_{for} = \mathbf{AS} \tag{3}$$

$$\mathbf{Z}_{free} = \mathbf{Z} - \mathbf{AS} \tag{4}$$

$$\mathbf{S}_{for} = \mathbf{BZ} \tag{5}$$

$$\mathbf{S}_{free} = \mathbf{S} - \mathbf{BZ} \tag{6}$$

Following Catalano et al. (2016)[84] the **Z** and **S** forced fields were further decomposed into fully coupled manifolds by substituting Eqs. 3–6 into Eqs. 1, 2 as below,

$$\mathbf{Z} = \mathbf{A}(\mathbf{BZ} + \mathbf{S}_{free}) + \mathbf{Z}_{free} = \mathbf{ABZ} + \mathbf{AS}_{free} + \mathbf{Z}_{free} \tag{7}$$

$$\mathbf{S} = \mathbf{B}(\mathbf{AS} + \mathbf{Z}_{free}) + \mathbf{S}_{free} = \mathbf{BAS} + \mathbf{BZ}_{free} + \mathbf{S}_{free} \tag{8}$$

In Eqs. 7 and 8, the **ABZ** and **BAS** are fully coupled manifolds of **Z** and **S** fields. These fully coupled manifolds' underlying mechanism could either be external forcing affecting both **S** and **Z** fields or mutual interactions between **S** and **Z** fields. The fully coupled manifolds ratio is further tested for significance using Monte Carlo simulations[83] of 1000 repetitions with a significance bound of 99%, assuring confidence in the variance retrieved.

$$\hat{\mathbf{Z}} = (\mathbf{ZZ}')^{-1/2} \tag{9}$$

$$\hat{\mathbf{S}} = (\mathbf{SS}')^{-1/2} \tag{10}$$

We first calculated the principal components (EOF) of the respective climate fields (**Z** and **S**) that have retained 99% of each input field's total variance. The EOF technique[85,86] decomposes a climate parameter into an independent, uncorrelated set of orthogonal eigenvectors; principally, the leading mode explains most of the variance, followed by the second mode. The EOF methods presume that a homogenously dimensioned data matrix (**X**) has many dominant modes of variability in Euclidian space[87]. Thus, the eigenvectors e_j of the covariance matrix of data **X**, ($\mathbf{X}^T\mathbf{X}$) produce an orthogonal basis for dataset **X**, as shown in Eq. 11.

$$(\mathbf{X}(m,n)) = \sum_{j=1}^{y} \mathbf{a}_j(m)\mathbf{e}_j(n) \tag{11}$$

where $\mathbf{a}_j$ denotes the principal component, which can be termed the temporal weight of $\mathbf{e}_j$ ($\mathbf{e}_j$) represents the eigenvector of the covariance matrix in the spatial domain. The principal components obtained are uncorrelated to each other, and their variance is equal to that of $\mathbf{e}_j$. The variance's significance is tested using a student t-test[28] with a confidence bound of 99 %. The Canonical Correlation Analysis (CCA)[49] is applied to scale principal components of the two climate fields before Procrustes minimization, as shown in Eqs. 7 and 8. The **Ž** and **Š** fields in the given equations are CCA-scaled principal components used in CMT calculation.

Previously studies have used this approach to coupled land-atmosphere and ocean studies[28,32,49].

Divergent wind

The divergent wind contributes >30% to the total wind field in the deep tropics and subtropical climate[88]. It significantly impacts the vertical motion, diabatic heating, precipitation, and atmospheric energetics in tropical and subtropical climates[88–90]. Using Helmholtz theorem, the horizontal wind field $\mathbf{v} = (u, v)$ can be decomposed into stream function ($\mathbf{v}_\psi$) and velocity potential ($\mathbf{v}_\chi$) as,

$$\mathbf{v} = (\mathbf{k} \times \nabla_\psi + \nabla_\chi) \equiv \mathbf{v}_\psi + \mathbf{v}_\chi \tag{12}$$

In Eq. 12, k denotes the unit vector in the vertical direction and ∇ is the gradient operator in a two-dimensional space (x, y).

Vertically Integrated Moisture Flux

In the atmospheric water balance, MFC is an essential component and can be expressed in Eqs. 13 and 14 as,

$$dQ/dt = E - P + \text{MFC} \tag{13}$$

$$\text{MFC} = -\frac{1}{g} \nabla . \int_0^{Ps} q\, \vec{\mathbf{V}} dp \tag{14}$$

In the above equations[91], Q is the atmospheric column of water, t is time, E is evapotranspiration, P is precipitation and MFC is vertically integrated moisture flux, g is the gravitational acceleration, Ps is surface pressure, q is specific humidity, $\vec{\mathbf{V}}$ is wind components (both $\mathbf{u}$ & $\mathbf{v}$), and p is the upper limit of the atmospheric pressure field.

Regional climate model and experiments

We used the ICTP regional climate model RegCM (RegCM4, version 4.7.0) coupled with the Biosphere-Atmosphere Transfer Scheme (BATS) land surface model, which comes with three soil moisture layers of varying depth from the land surface to 3 m deep[92,93]. The soil moisture quantity of each layer (surface to 0.1 m, surface to 1 m, and surface to 3 m) is represented by soil water contents (kg m^{-2}) of each layer. Here, we rely on the Emanuel cumulus convection scheme[94] over land and a sub-grid cloud and precipitation scheme (SUBEX), which accounts for large-scale rainfall[95] in the parameterization physics of the model. ERA-interim datasets were used to provide both lateral boundary conditions (6-hourly) and sea surface temperature (SST) forcings (weekly) for the experiments. Over land, BATS, which has been used in both offline and coupled (to other atmospheric models) modes to represent land surface contributions to the region-specific-scale energy and water budgets[96,97], is also chosen here because of its coherence to the classic hydrological framework[30]. Since ECV SM only represents the surface estimates, profiles for the three layers of BATS were obtained following (Bisselink et al. 2011)[98]. We also note here that since we used the same SST forcings for both experiments, their difference can be reliably associated with changes in soil moisture[61,99]. The SM of the first time-step of each day is replaced with ECV SM anomalies (climatology), hereafter SM_{ECV} (SM_{CLIM}), complementing the hydrological, physical process-based framework[30,100]. We stress that our approach is process-oriented: we use these targeted, idealized model experiments (Supplementary Fig. 3a) to probe the role of SM variability and advance our understanding of monsoon precipitation sensitivity to SM across China. Our goal here is not to evaluate which simulation is more realistic in the context of absolute precipitation variability. In the real physical world, the dynamic sensitivity of SM impacts the overlying atmosphere through energy fluxes; thus, in the current simulation, SM_{ECV}

should be considered more realistic. The control and sensitivity experiment covered the 2000–2018 period when the ECV SM benefited from a maximum number of input data products[74]. Therefore, to ensure that the best quality of SM is being used to drive the model, we choose 2000–2018 as the control and sensitivity experiment duration, whereas 1998–1999 are used as spinup years for the model. The precipitation and atmospheric variables from 2000 to 2018 are compared with the Chinese Meteorological Administration (CMA) precipitation and ERA5 reanalysis product. The pattern-based statistics of the SM_{ECV} simulations are shown (Supplementary Fig. 3b) using the Taylor diagram[101], including the precipitation, PBL, 2-m temperature, LH, and SH of the EAM domain (Supplementary Fig. 3a) and 500 hPa vertical velocity, and wind components of the model domain. Both land surface and atmospheric variables interannual variability in SM_{ECV} run is reasonably produced with correlation >55%, relatively smaller amplitude deviation (STD: <1.30), and unbiased differences (ubRMSD: <0.80).

REFERENCES

1. Zhu, S. et al. Distinct impacts of spring soil moisture over the Indo-China Peninsula on summer precipitation in the Yangtze River basin under different SST backgrounds. *Clim. Dyn.* **56**, 1895–1918 (2021).
2. Shi, P. et al. Significant land contributions to interannual predictability of East Asian summer monsoon rainfall. *Earth's Futur* **9**, 1–16 (2021).
3. Wu, G. et al. Thermal controls on the Asian summer monsoon. *Sci. Rep.* **2**, 404 (2012).
4. Wei, W., Zhang, R., Wen, M., Rong, X. & Li, T. Impact of Indian summer monsoon on the South Asian High and its influence on summer rainfall over China. *Clim. Dyn.* **43**, 1257–1269 (2014).
5. Wang, B., Xiang, B. & Lee, J. Y. Subtropical High predictability establishes a promising way for monsoon and tropical storm predictions. *Proc. Natl Acad. Sci. USA* **110**, 2718–2722 (2013).
6. Kundzewicz, Z. W. et al. Climate variability and floods in China—a review. *Earth-Sci. Rev.* **211**, 103434 (2020).
7. Wang, C., Yang, K., Li, Y., Wu, D. & Bo, Y. Impacts of spatiotemporal anomalies of Tibetan plateau snow cover on summer precipitation in Eastern China. *J. Clim.* **30**, 885–903 (2017).
8. Ding, T. & Gao, H. Relationship between winter snow cover days in Northeast China and rainfall near the Yangtze river basin in the following summer. *J. Meteorol. Res.* **29**, 400–411 (2015).
9. Kundzewicz, Z. W. et al. Flood risk and its reduction in China. *Adv. Water Resour.* **130**, 37–45 (2019).
10. Jiang, T. et al. Each 0.5 °C of warming increases annual flood losses in China by more than US$60 billion. *Bull. Am. Meteorol. Soc.* **101**, E1464–E1474 (2021).
11. Su, B. et al. Drought losses in China might double between the 1.5 and 2.0 °C warming. *Proc. Natl Acad. Sci. USA* **115**, 10600–10605 (2018).
12. Li, Z., Sun, Y., Li, T., Ding, Y. & Hu, T. Future Changes in East Asian Summer Monsoon Circulation and Precipitation Under 1.5 to 5 °C of Warming. *Earth's Futur* **7**, 1391–1406 (2019).
13. Zhang, R. H. Natural and human-induced changes in summer climate over the East Asian Monsoon region in the last half century: a review. *Adv. Clim. Chang. Res.* **6**, 131–140 (2015).

14. Almazroui, M. et al. Projected changes in climate extremes using CMIP6 simulations over SREX regions. *Earth Syst. Environ.* **5**, 481–497 (2021).

15. Huang, J. J., Zhang, N., Choi, G., McBean, E. A. & Zhang, Q. Spatiotemporal patterns and trends of precipitation and their correlations with related meteorological factors by two sets of reanalysis data in China. *Hydrol. Earth Syst. Sci. Discuss* **5**, 1–35 (2018).

16. Ha, K. J., Heo, K. Y., Lee, S. S., Yun, K. S. & Jhun, J. G. Variability in the East Asian Monsoon: a review. *Meteorol. Appl.* **19**, 200–215 (2012).

17. Wang, P. X. et al. The global monsoon across time scales: Mechanisms and outstanding issues. *Earth-Sci. Rev.* **174**, 84–121 (2017).

18. Wu, G. et al. The influence of mechanical and thermal forcing by the Tibetan Plateau on Asian climate. *J. Hydrometeorol.* **8**, 770–789 (2007).

19. Abe, M., Hori, M., Yasunari, T. & Kitoh, A. Effects of the Tibetan Plateau on the onsetof the summer monsoon in South Asia: The role of the air-sea interaction. *J. Geophys. Res. Atmos.* **118**, 1760–1776 (2013).

20. Abbas, A., Waseem, M., Ullah, W., Zhao, C. & Zhu, J. Spatiotemporal analysis of meteorological and hydrological droughts and their propagations. *Water* **13**, 2237 (2021).

21. Zhu, C., Lee, W. S., Kang, H. & Park, C. K. A proper monsoon index for seasonal and interannual variations of the East Asian Monsoon. *Geophys. Res. Lett.* **32**, 1–5 (2005).

22. Wu, L. & Zhang, J. The relationship between spring soil moisture and summer hot extremes over North China. *Adv. Atmos. Sci.* **32**, 1660–1668 (2015).

23. Gao, C. et al. Land–atmosphere interaction over the Indo-China Peninsula during spring and its effect on the following summer climate over the Yangtze River basin. *Clim. Dyn.* **53**, 6181–6198 (2019).

24. Wang, B. & Fan, Z. Choice of South Asian summer monsoon indices. *Bull. Am. Meteorol. Soc.* **80**, 629–638 (1999).

25. Lv, A., Qu, B., Jia, S. & Zhu, W. Influence of three phases of El Niño-Southern Oscillation on daily precipitation regimes in China. *Hydrol. Earth Syst. Sci.* **23**, 883–896 (2019).

26. Wu, Z., Li, J., Jiang, Z. & Ma, T. Modulation of the Tibetan Plateau snow cover on the ENSO teleconnections: from the East Asian summer monsoon perspective. *J. Clim.* **25**, 2481–2489 (2012).

27. Liu, D., Wang, G., Mei, R., Yu, Z. & Yu, M. Impact of initial soil moisture anomalies on climate mean and extremes over Asia. *J. Geophys. Res.* **119**, 529–545 (2014).

28. Ullah, W. et al. Observed linkage between Tibetan plateau soil moisture and South Asian summer precipitation and the possible mechanism. *J. Clim.* **34**, 361–377 (2021).

29. Koster, R. D., Chang, Y., Wang, H. & Schubert, S. D. Impacts of local soil moisture anomalies on the atmospheric circulation and on remote surface meteorological fields during boreal summer: a comprehensive analysis over North America. *J. Clim.* **29**, 7345–7364 (2016).

30. Seneviratne, S. I. et al. Investigating soil moisture-climate interactions in a changing climate: a review. *Earth-Sci. Rev.* **99**, 125–161 (2010).

31. Mei, R. & Wang, G. Impact of sea surface temperature and soil moisture on summer precipitation in the united states based on observational data. *J. Hydrometeorol.* **12**, 1086–1099 (2011).

32. Alessandri, A. & Navarra, A. On the coupling between vegetation and rainfall inter-annual anomalies: possible contributions to seasonal rainfall predictability over land areas. *Geophys. Res. Lett.* **35**, 1–6 (2008).

33. Dorigo, W. et al. ESA CCI soil moisture for improved Earth system understanding: state-of-the art and future directions. *Remote Sens. Environ.* **203**, 185–215 (2017).

34. Santanello, J. A. et al. Land-atmosphere interactions the LoCo perspective. *Bull. Am. Meteorol. Soc.* **99**, 1253–1272 (2018).

35. Rasmijn, L. M. et al. Future equivalent of 2010 Russian heatwave intensified by weakening soil moisture constraints. *Nat. Clim. Chang.* **8**, 381–385 (2018).

36. Denissen, J. M. C. et al. Soil moisture signature in global weather balloon soundings. *npj Clim. Atmos. Sci.* **4**, 13 (2021).

37. Lau, W. K. M. & Kim, K. M. The 2010 Pakistan flood and Russian heat wave: teleconnection of hydrometeorological extremes. *J. Hydrometeorol.* **13**, 392–403 (2012).

38. Mann, M. E. et al. Influence of anthropogenic climate change on planetary wave resonance and extreme weather events. *Sci. Rep.* **7**, 12 (2017).

39. Miralles, D. G., Teuling, A. J., Van Heerwaarden, C. C. & De Arellano, J. V. G. Mega-heatwave temperatures due to combined soil desiccation and atmospheric heat accumulation. *Nat. Geosci.* **7**, 345–349 (2014).

40. Dong, X., Zhou, Y., Chen, H., Zhou, B. & Sun, S. Lag impacts of the anomalous July soil moisture over Southern China on the August rainfall over the Huang–Huai River Basin. *Clim. Dyn.* **58**, 1737–1754 (2022).

41. Bao, Q., Liu, Y., Shi, J. & Wu, G. Comparisons of soil moisture datasets over the Tibetan Plateau and application to the simulation of Asia summer monsoon onset. *Adv. Atmos. Sci.* **27**, 303–314 (2010).

42. Meng, X. et al. Detecting hydrological consistency between soil moisture and precipitation and changes of soil moisture in summer over the Tibetan Plateau. *Clim. Dyn.* **51**, 4157–4168 (2018).

43. Wei, J. & Dirmeyer, P. A. Sensitivity of land precipitation to surface evapotranspiration: a nonlocal perspective based on water vapor transport. *Geophys. Res. Lett.* **46**, 12588–12597 (2019).

44. Wei, J. & Dirmeyer, P. A. Dissecting soil moisture-precipitation coupling. *Geophys. Res. Lett.* **39**, 1–6 (2012).

45. Kim, Y. & Wang, G. Soil moisture-vegetation-precipitation feedback over North America: its sensitivity to soil moisture climatology. *J. Geophys. Res. Atmos.* **117**, 1–18 (2012).

46. Ullah, W., Wang, G., Gao, Z., Hagan, D. F. T. & Lou, D. Comparisons of remote sensing and reanalysis soil moisture products over the Tibetan Plateau, China. *Cold Reg. Sci. Technol.* **146**, 110–121 (2018).

47. Samuel, J., Coulibaly, P., Dumedah, G. & Moradkhani, H. Assessing model state and forecasts variation in hydrologic data assimilation. *J. Hydrol.* **513**, 127–141 (2014).

48. Koster, R. D. et al. Regions of strong coupling between soil moisture and precipitation. *Science* **305**, 1138–1140 (2004).

49. Navarra, A. & Tribbia, J. The coupled manifold. *J. Atmos. Sci.* **62**, 310–330 (2005).

50. Kottek, M., Grieser, J., Beck, C., Rudolf, B. & Rubel, F. World map of the Köppen–Geiger climate classification updated. *Meteorol. Z.* **15**, 259–263 (2006).

51. Liu, B. et al. Asian summer monsoon onset barrier and its formation mechanism. *Clim. Dyn.* **45**, 711–726 (2015).

52. Liu, B., Wu, G., Mao, J. & He, J. Genesis of the South Asian high and its impact on the Asian summer monsoon onset. *J. Clim.* **26**, 2976–2991 (2013).

53. Li, J. et al. How to measure the strength of the East Asian Summer monsoon. *J. Clim.* **21**, 4449–4463 (2008).

54. Wang, B., LinHo, Zhang, Y. & Lu, M. M. Definition of South China Sea monsoon onset and commencement of the East Asian summer monsoon. *J. Clim.* **17**, 699–710 (2004).

55. Xing, N., Li, J. & Wang, L. Effect of the early and late onset of summer monsoon over the Bay of Bengal on Asian precipitation in May. *Clim. Dyn.* **47**, 1961–1970 (2016).

56. Khan, A. A. et al. Spatial and temporal analysis of rainfall and drought condition in Southwest Xinjiang in Northwest China, using various climate indices. *Earth Syst. Environ.* **5**, 201–216 (2021).

57. Zhang, Z., Sun, X. & Yang, X.-Q. Understanding the interdecadal variability of East Asian summer monsoon precipitation: joint influence of three oceanic signals. *J. Clim.* **31**, 5485–5506 (2018).

58. Liu, L., Zhang, R. & Zuo, Z. Effect of spring precipitation on summer precipitation in Eastern China: role of soil moisture. *J. Clim.* **30**, 9183–9194 (2017).

59. Chahine, M. T. The hydrological cycle and its influence on climate. *Nature* **359**, 373–380 (1992).

60. Zhang, R. & Zuo, Z. Impact of spring soil moisture on surface energy balance and summer monsoon circulation over East Asia and precipitation in East China. *J. Clim.* **24**, 3309–3322 (2011).

61. Berg, A., Lintner, B., Findell, K. & Giannini, A. Soil moisture influence on seasonality and large-scale circulation in simulations of the West African monsoon. *J. Clim.* **30**, 2295–2317 (2017).

62. Taylor, C. M. et al. New perspectives on land-atmosphere feedbacks from the African monsoon multidisciplinary analysis. *Atmos. Sci. Lett.* **12**, 38–44 (2011).

63. Zuo, Z. & Zhang, R. Influence of soil moisture in eastern China on the East Asian summer monsoon. *Adv. Atmos. Sci.* **33**, 151–163 (2016).

64. Yang, K., Wang, C. & Bao, H. Contribution of soil moisture variability to summer precipitation in the northern hemisphere. *J. Geophys. Res.* **121**, 12,108–12,214 (2016).

65. Min, J., Guo, Y. & Wang, G. Impacts of soil moisture on typical frontal rainstorm in Yangtze River Basin. *Atmosphere* **7**, 0–24 (2016).

66. Zhu, B., Xie, X., Meng, S., Lu, C. & Yao, Y. Sensitivity of soil moisture to precipitation and temperature over China: present state and future projection. *Sci. Total Environ.* **705**, 135774 (2020).

67. Cheng, S., Guan, X., Huang, J., Ji, F. & Guo, R. Long-term trend and variability of soil moisture over East Asia. *J. Geophys. Res.* **120**, 8658–8670 (2015).

68. AbdelRahman, M. A. E. & Arafat, S. M. An approach of agricultural courses for soil conservation based on crop soil suitability using geomatics. *Earth Syst. Environ.* **4**, 273–285 (2020).

69. Liu, Y. et al. Agriculture intensifies soil moisture decline in Northern China. *Sci. Rep.* **5**, 11261 (2015).

70. Yuan, Q. et al. Coupling of soil moisture and air temperature from multiyear data during 1980–2013 over china. *Atmosphere* **11**, 0–14 (2020).

71. Xu, Z., Chen, H., Guo, J. & Zhang, W. Contrasting effect of soil moisture on the daytime boundary layer under different thermodynamic conditions in summer over China. *Geophys. Res. Lett.* **48**, 1–11 (2021).

72. Xia, K., Li, L., Tang, Y. & Wang, B. Impact of soil freezing-thawing processes on August rainfall over Southern China. *J. Geophys. Res. Atmos.* **127**, 1–16 (2022).

73. Gu, X. et al. Extreme precipitation in China: a review on statistical methods and applications. *Adv. Water Resour.* **163**, 104144 (2022).

74. Karthikeyan, L., Pan, M., Wanders, N., Kumar, D. N. & Wood, E. F. Four decades of microwave satellite soil moisture observations: Part 2. Product validation and inter-satellite comparisons. *Adv. Water Resour.* **109**, 236–252 (2017).

75. Yuan, Z., Yang, Z., Yan, D. & Yin, J. Historical changes and future projection of extreme precipitation in China. *Theor. Appl. Climatol.* **127**, 393–407 (2017).

76. Ren, Z. et al. Changes in daily extreme precipitation events in South China from 1961 to 2011. *J. Geogr. Sci.* **25**, 58–68 (2015).

77. Dorigo, W. A. et al. Evaluation of the ESA CCI soil moisture product using ground-based observations. *Remote Sens. Environ.* **162**, 380–395 (2015).

78. Wang, G., Garcia, D., Liu, Y., de Jeu, R. & Dolman, A. J. A three-dimensional gap filling method for large geophysical datasets: application to global satellite soil moisture observations. *Environ. Model. Softw.* **30**, 139–142 (2012).

79. Hersbach, H. et al. Global reanalysis: goodbye ERA-Interim, hello ERA5. *ECMWF Newsl.* 17–24 (2019).

80. Hersbach, H. et al. The ERA5 global reanalysis. *Q. J. R. Meteorol. Soc.* **146**, 1999–2049 (2020).

81. Hagan, D. F. T., Parinussa, R. M., Wang, G. & Draper, C. S. An evaluation of soil moisture anomalies from global model-based datasets over the People's Republic of China. *Water* **12**, 1–15 (2020).

82. Richman, M. B. & Vermette, S. J. The use of procrustes target analysis to discriminate dominant source regions of fine sulfur in the western USA. *Atmos. Environ. Part A. Gen. Top.* **27**, 475–481 (1993).

83. Wang, G., Dolman, A. J. & Alessandri, A. A summer climate regime over Europe modulated by the North Atlantic Oscillation. *Hydrol. Earth Syst. Sci.* **15**, 57–64 (2011).

84. Catalano, F., Alessandri, A., De Felice, M., Zhu, Z. & Myneni, R. B. Observationally based analysis of land-atmosphere coupling. *Earth Syst. Dyn.* **7**, 251–266 (2016).

85. Hannachi, A. *A primer for EOF analysis of climate data.* (United Kingdom: Department of Meteorology, University of Reading, 2004).

86. Lund, R. B., von Storch, H. & Zwiers, F. W. Statistical analysis in climate research. *J. Am. Stat. Assoc.* **95**, 1375 (2000).

87. Preisendorfer, R. W. *Principal Component Analysis in Meteorology and Oceanography* XVIII, 425 (Elsevier; Distributors for the U.S. and Canada, Elsevier Science Pub. Co., 1988).

88. Krishnamurti, T. N. Tropical East-West circulations during the Northern summer. *J. Atmos. Sci.* **28**, 1342–1347 (1971).

89. Mancuso, R. L. A numerical procedure for computing fields of stream function and velocity potential. *J. Appl. Meteorol.* **6**, 994–1001 (1967).

90. Kulkarni, P. L., Mitra, A. K., Narkhedkar, S. G., Bohra, A. K. & Rajamani, S. On the impact of divergent part of the wind computed from INSAT OLR data on global analysis and forecast fields. *Meteorol. Atmos. Phys.* **64**, 61–82 (1997).

91. Wei, J., Su, H. & Yang, Z. L. Impact of moisture flux convergence and soil moisture on precipitation: a case study for the southern United States with implications for the globe. *Clim. Dyn.* **46**, 467–481 (2016).

92. Pal, J. S. et al. Regional Climate Modeling for the Developing World: The ICTP RegCM3 and RegCNET. *Bull. Am. Meteorol. Soc.* **88**, 1395–1410 (2007).

93. Dickinson, R. E., Henderson-Sellers, A. & Kennedy, P. J. *Biosphere-atmosphere Transfer Scheme (BATS) Version 1e as Coupled to the NCAR Community Climate Model* (No. NCAR/TN-387+STR). (University Corporation for Atmospheric Research, 1993). https://doi.org/10.5065/D67W6959.

94. Emanuel, K. A. A scheme for representing cumulus convection in large-scale models. *J. Atmos. Sci.* **48**, 2313–2329 (1991).

95. Pal, J. S., Small, E. E. & Eltahir, E. A. B. Simulation of regional-scale water and energy budgets: representation of subgrid cloud and precipitation processes within RegCM. *J. Geophys. Res. Atmos.* **105**, 29579–29594 (2000).

96. Dirmeyer, P. A., Zeng, F. J., Ducharne, A., Morrill, J. C. & Koster, R. D. The sensitivity of surface fluxes to soil water content in three land surface schemes. *J. Hydrometeorol.* **1**, 121–134 (2000).

97. Wei, J., Dickinson, R. E. & Chen, H. A negative soil moisture–precipitation relationship and its causes. *J. Hydrometeorol.* **9**, 1364–1376 (2008).

98. Bisselink, B., van Meijgaard, E., Dolman, A. J. & de Jeu, R. A. M. Initializing a regional climate model with satellite-derived soil moisture. *J. Geophys. Res. Atmos.* **116**, 1–13 (2011).

99. Yang, K. & Wang, C. Seasonal persistence of soil moisture anomalies related to freeze–thaw over the Tibetan Plateau and prediction signal of summer precipitation in eastern China. *Clim. Dyn.* **53**, 2411–2424 (2019).

100. Dickinson, R. E., Errico, R. M., Giorgi, F. & Bates, G. T. A regional climate model for the western United States. *Clim. Change* **15**, 383–422 (1989).

101. Taylor, K. E. Summarizing multiple aspects of model performance in a single diagram. *J. Geophys. Res. Atmos.* **106**, 7183–7192 (2001).

ACKNOWLEDGEMENTS

AUTHOR CONTRIBUTIONS

W.U. and G.W.: Conceptualization; D.F.T.H., J.W., Z.C., and L.S.: Data curation; W.U., D.L., and D.F.T.H.: Formal analysis; G.W.: Funding acquisition; W.U., D.F.T.H., J.W., and Z.C.: Methodology; G.W., S.B., and J.T.: Project administration, resources, software, and supervision; W.U. and D.F.T.H.: Validation, visualization; W.U., and D.F.T.H.: Writing - original draft; W.U., G.W., A.K.: Writing - review & editing.

COMPETING INTERESTS

The authors declare no competing interests.

ADDITIONAL INFORMATION

Supplementary information The online version contains supplementary material available at https://doi.org/10.1038/s41612-023-00331-4.

Correspondence and requests for materials should be addressed to Guojie Wang.

Reprints and permission information is available at http://www.nature.com/reprints

Publisher's note Springer Nature remains neutral with regard to jurisdictional claims in published maps and institutional affiliations.